The Report Committee for Kevin Michael Martinez
Certifies that this is the approved version of the following report:

Considerations in Conducting Adhesion Experiments via Nanoindentation

APPROVED BY
SUPERVISING COMMITTEE:

Supervisor:

Kenneth Liechti

Rui Huang

Considerations in Conducting Adhesion Experiments via Nanoindentation

by

Kevin Michael Martinez

Report

Presented to the Faculty of the Graduate School of

The University of Texas at Austin

in Partial Fulfillment

of the Requirements

for the Degree of

Master of Science in Engineering

The University of Texas at Austin

December 2017

Acknowledgements

To my advisor, Dr. Liechti, for his continuous support and guidance over the last two and a half years. My graduate studies would have been a lesser experience without your mentorship.

To the engineering staff at Hysitron for their never-ending support over the past five years in both my industry and academic pursuits. Without our work together at Samsung, I may have never continued on to graduate school. I owe all of you a debt of thanks: Lance Kuhn, Doug Stauffer, Ronnie Cooper, Jacob Noble and Jacob Fredrickson.

To Mike Fitzl for always answering the phone. Working with you over the past five years has been a true pleasure, made even more so by your friendship. You and Mandy always have a place to stay, wherever I might be.

To my girlfriend Hannah, for her understanding over this past year and always waiting oh so patiently. The lab at Pickle was never illuminated as brightly without your presence.

And finally, to all my family, for your endless love and long-distance support during the Austin experience. All my success is owed to you.

Abstract

Considerations in Conducting Adhesion Experiments via Nanoindentation

Kevin Michael Martinez, M.S.E.
The University of Texas at Austin, 2017

Supervisor: Kenneth Liechti

Recent attempts to commercialize graphene-based technology for flexible electronics applications have largely failed due to a lack of scalable, cost effective graphene transfer options. Dry graphene R2R transfer processes have numerous advantages over wet processes, but their development requires further characterization of the graphene-substrate interfaces. In support of this initiative, a displacement-controlled nanoindenter experimental protocol was developed for characterizing adhesion interactions between a diamond probe and specimen substrate surface. This protocol was used to characterize probe interactions with quartz, graphite, and silicon samples in ambient and nitrogen environments. Available literature data for diamond probe-silicon interactions correspond well to our work. However, persistent adhesive snap-behavior due to motor control deficiency in the selected device significantly reduced the utility of this technique. Resolution of full interaction behavior is severely impacted and is reduced to the order of 5 nm from the stated transducer capability of 0.4 nm.

Table of Contents

Chapter 1: Introduction 1
1.1 Flexible Electronics and Graphene 1
1.2 Molecular Adhesion 4
1.3 Research Motivation and Objectives 6
1.4 Proposed Method 6
1.5 Thesis Organization 7

Chapter 2: Literature Review 8
2.1 Graphene Adhesion Studies 8
2.1.1 Blister Test 9
2.1.2 Beam Fracture Test 10
2.1.3 Nanoindentation 10
2.2 Instrumented Techniques for Interfacial Characterization 11
2.2.1 Surface Force Apparatus 11
2.2.2 Atomic Force Microscopy 13
2.2.3 Interfacial Force Microscopy 14
2.2.4 Nanoindenter 15

Chapter 3: Theory 17
3.1 Elastic Contact Mechanics 17

Chapter 4: Experimental Technique 21
4.1 Overview 21
4.2 Motor Control 22
4.2.1 Open-Loop Control 23
4.2.2 Load Control 24
4.2.3 Displacement Control 24
4.3 Error Mitigation 26
4.3.1 Thermal Error 26
4.3.2 System Error – Initial Penetration 28
4.3.3 System Error – Displacement Control 29

4.3.4 Hardware Error – Probe Surface Condition....35

Chapter 5: Results....37

5.1 Overview....37

5.2 Fused-Silica....38

5.3 Graphite....40

5.4 Silicon....42

Chapter 6: Summary and Future Work....47

6.1 Thesis Summary....47

6.2 Future Work....49

Appendix....50

Appendix: DMT Contact Validation....50

References....55

Chapter 1: Introduction

1.1 Flexible Electronics and Graphene

The field of flexible electronics has been under continuous development for more than fifty years. The concept of flexible devices was born of the powerful realization that many conventional devices could be given increased compliance by thinning the device carrier substrate and mounting on a flexible support backing. Solar cells were the first device to be made flexible in 1967, using single crystal silicon wafers that had been thinned to 100 µm and mounted on a plastic backing (Crabb and Treble, 1967). Flexible thin-film-transistors (TFT) arrived one year later in 1968, using a Tellurium film deposited on a strip of paper (Brody, 1984). Subsequent decades saw extensive research into characterizing silicon-based TFTs on a variety of flexible substrates (Wong and Salleo, 2009).

Figure 1.1: (Left) Demonstration of Samsung Youm prototype (CES Conference 2013)
(Right) Galaxy Round device (Samsung)

However, it was not until the mid-21st century that flexed displays and sensors first arrived on the consumer market courtesy of Samsung, Sony, and LG. Within the past ten years, all three companies have released mass production television displays using flexible OLED technology. In 2013, Samsung was the first company to implement the

technology in mass production smartphones, the Galaxy Round and Galaxy Edge line (see Figure 1.1). All three companies are continuing to work on products that will be nonrigid and allow active display motion.

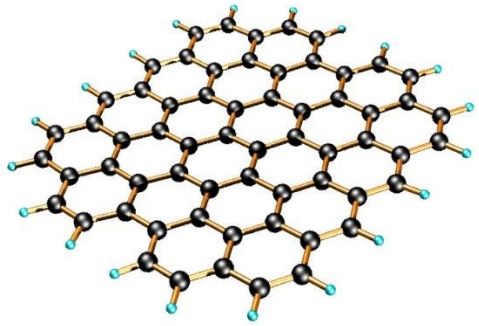

Figure 1.2: Graphene hexagonal carbon structure (cnx.org)

Since its discovery in 2004, graphene's extraordinary material properties have galvanized many new semiconductor device research ventures. This material is particularly attractive for flexible electronics applications as a carrier substrate due to exceptional physical and electrical properties. Graphene's mono-atomic layer structure provides excellent flexibility and transparency, while its triple covalent carbon bonds create high in-plane stiffness approaching one terapascal. Studies have shown that graphene has excellent charge carrier mobility with speeds up to hundred times that of silicon (Bolotin et al., 2008). In addition to its exceptional carrier substrate characteristics, graphene is roll-to-roll (R2R) compatible as it can be grown in large area sheets.

R2R processing is utilized extensively in electronic device manufacturing due to excellent economies of scale. In a typical R2R transfer device, large-area graphene is separated from the growth foil and transferred to a target substrate selected for processing manufacturability (see Figure 1.3). Separation is generally achieved through a wet

chemical etch process where the growth foil is dissolved. The graphene is then left on the target substrate and device processing can begin.

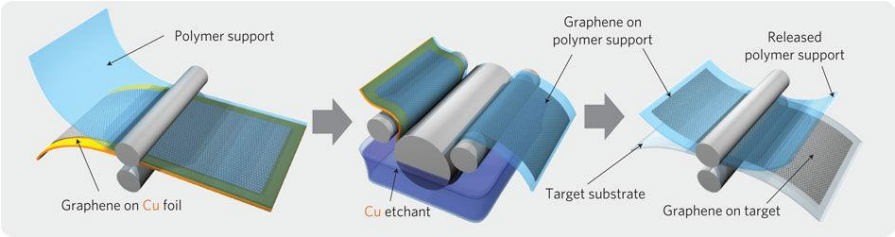

Figure 1.3: Prototype R2R graphene transfer device, production rate of 150mm/min (Sukang et al., 2010)

Electronics manufacturers (Sony, Samsung) have developed working R2R graphene transfer prototypes, but the technology is not yet cost effective. The wet chemical etch step driving the transfer process greatly impacts process scalability and is expensive. The typical growth substrate medium for graphene is pure copper, which must be totally dissolved during the etch process, a relatively time-consuming process that reduces manufacturing scalability. Furthermore, following dissolution the copper foil is non-reusable significantly increasing process costs.

In an attempt to address the scalability and cost issues associated with graphene wet transfer processes, the NASCENT group at UT-Austin is currently developing a new R2R graphene transfer process (see Figure 1.4). During device operation, the target polymer will be applied to the graphene surface, forming a copper-graphene-polymer stack. A dry mechanical delamination step will then peel the graphene from the copper substrate, leaving graphene on the polymer substrate. Further transfer steps will be simplified by selecting for polymer materials which only bond to graphene through dispersive adhesion.

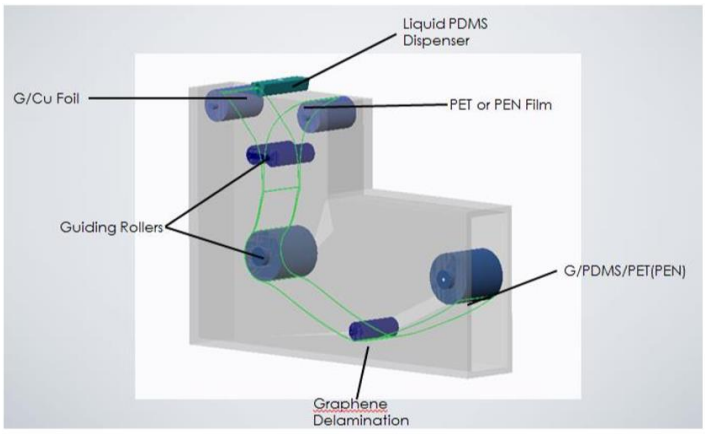

Figure 1.4: Conceptual design for NASCENT group R2R graphene transfer device (Xin, 2013)

Further characterization of the graphene and growth/target substrate interfaces is required to guide the R2R design process. Preferential delamination between the graphene and copper layer will only occur if the interface toughness or strength is less than that of graphene and polymer layer. The surface forces and interactions between all layers are governed by intermolecular adhesion mechanisms, whose characteristics must be experimentally determined through the full range of separation.

1.2 Molecular Adhesion

Adhesion is a general term liberally found through literature with a variety of meanings depending on the scientific context. Molecular adhesion or dispersion is generally used to refer to the action of interfacial surface forces across an interface separating two bodies. These interfacial forces are characterized by distinct magnitudes and interaction ranges depending on underlying mechanisms. For dispersion, the primary mechanism is intermolecular secondary bonding acting through hydrogen bonding or van der Waal (vdW) interactions.

Hydrogen bonds are intermediate strength bonds with energy levels between stronger primary bonds and weaker vdW interactions. They result from the electrostatic attraction between hydrogen atoms and "neighboring" atoms with relatively high electronegativity. Typical interfacial force magnitudes and interaction ranges for secondary bonding mechanisms can be seen in Figure 1.5.

Bond type	Bond energy kJ mol^{-1}	Equilibrium length nm
Primary, chemical		
Ionic	600–1000	0.2–0.4
Covalent	60–800	0.1–0.3
Metallic	100–350	0.2–0.6
Acid-base interactions		
Conventional Brønsted	<1000	
Lewis	<80	
Secondary, physical		
Hydrogen	~50	0.3
Van der Waals		
Dipole interactions	5–20	0.4
London, dispersion	1–40	<1

Figure 1.5: Bond energies and operating length scales (Rigby et al., 1986)

Van der Waal interactions are markedly more complex phenomena, which may be further broken down into polar or dispersion interactions. Polar interfacial forces are the result of permanent or induced dipole interactions, requiring the interaction of polar molecules. Dispersion is a fundamental atomic phenomenon that occurs within all materials. The strength and interaction range of dispersion forces varies considerably depending on the atomic actors involved. These fundamental forces result from instantaneous non-symmetry in electron orbital shells, which leads to a temporary dipole moment across the atom. This dipole moment can then interact with neighboring atoms by inducing dipoles and leading to electrostatic attraction.

Van der Waal interactions operate at sub-nanometer length scales and at energies that can be a small fraction of primary bonds. The atomic-scale nature of these

interactions makes experimental characterization difficult at nanometer and angstrom scale separation distances. Tabor and Winterton were the first to characterize the interaction range of two substrates below 100nm separation (Tabor and Winterton, 1969). Tabor continued their work to later establish the first dedicated instrument to measuring surface forces, the surface force apparatus (SFA) (Israelachvili et al., 1972). This proved to be the first of many conventional instrument platforms for characterizing the energy and interaction ranges of atomic scale adhesion between surfaces, which we shall discuss further in Section 2.2.

1.3 Research Motivation and Objectives

Graphene is the ultimate charge carrying substrate for the flexible electronics industry. With the ability to operate up to one hundred times the speed of conventional silicon TFTs, graphene-based transistors have the potential to transform the device field. However, successful commercialization of this technology mandates the existence of a cost-effective manufacturing method. Current industry prototype R2R-graphene-transfer systems rely on cost-inefficient wet etch transfer processes. The design of a functional dry transfer process would have the potential to drop graphene device fabrication costs to an industry acceptable standard. The development of a dry transfer process necessitates further experimental characterization of interfacial interactions between graphene on copper foil and target polymer substrates.

1.4 Proposed Method

A nanoindenter experimental protocol using a Hysitron Triboindenter was developed for characterizing adhesion interactions between a diamond probe and a target substrate surface. Within this protocol, various system parameters were explored in order to minimize error and non-repeatability, including motor control method and settings, test

displacement path, and stabilization periods. Initial samples with known literature adhesion behavior were used to calibrate system settings. DMT analysis was used to validate all contact measurement data and to calculate adhesion energy.

1.5 THESIS ORGANIZATION

Chapter 1 provides a brief history of the flexible electronics industry before delving into the advantages of graphene-based vs. silicon based devices for flexible applications. Following is a discussion of current research and industry efforts to create a scalable R2R graphene transfer process for flexible device fabrication. The concept of molecular adhesion is introduced as well as its relation to graphene transfer processes. In Chapter 2, experimental techniques for characterizing graphene adhesion interactions are reviewed. Several experimental platforms are selected for further in-depth critical review. In Chapter 3, contact mechanics theory as relating to nanoindentation adhesion measurements is reviewed. Chapter 4 provides an overview of the experimental protocol developed to perform nanoindentation adhesion measurements using UT-Austin's nanoindenter system. Common sources of error and mitigation techniques are discussed. Motor control approaches are critically reviewed. In Chapter 5, results from nanoindentation experiments on fused silica, graphite, and silicon are presented. Interaction behavior and peak adhesion energy (DMT) are reviewed and compared to literature. Chapter 6 summarizes the results of this research endeavor and provides recommendations for future work.

Chapter 2: Literature Review

2.1 Graphene Adhesion Studies

The purpose of adhesion experiments is to characterize the interfacial interactions between two surfaces, specifically the adhesion energy, strength and range of interaction. A reoccurring complication within this experimental domain is location dependent variability due to non-uniform surface conditions (Boddeti et al., 2013) (Akiwande et al., 2017). The variation of local surface characteristics such as surface roughness, chemical composition, and moisture result in differing interfacial interactions. This incongruence occurs within all popular techniques for graphene adhesion characterization and is a continuing challenge in field of adhesion studies. This section reviews graphene adhesion experimental techniques and relates current characterization progress of graphene on a variety of substrates.

The three most common methods of graphene adhesion study are beam fracture experiments, blister tests, and nanoindentation. All three methods facilitate the calculation of adhesion energy between surfaces, but only beam fracture and nanoindentation experiments allow the direct measurement of interaction length scale. Between these two methods, nanoindentation techniques allow the measurement of full interaction with a resolution two orders of magnitude larger than beam methods.

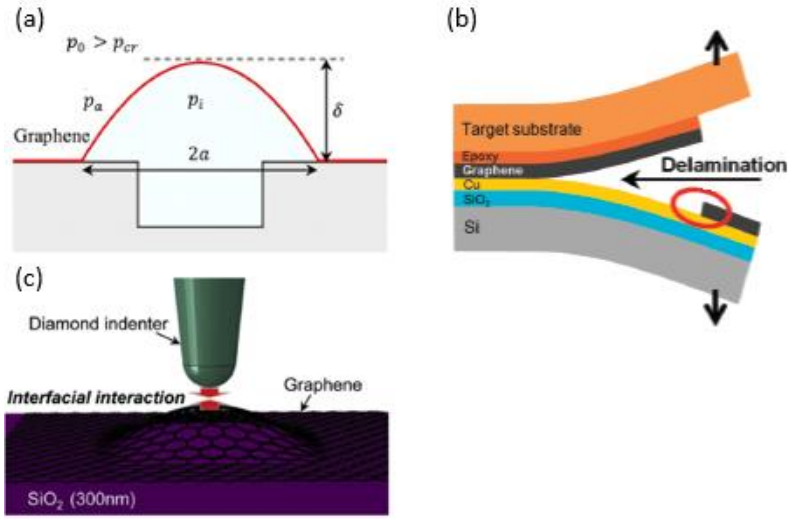

Figure 2.1: (a) Blister test diagram (Boddeti et al., 2013), (b) beam fracture layout (Yoon et al., 2012) and (c) nanoindentation via nanoindenter (Na et al., 2016)

2.1.1 Blister Test

Blister tests have been used to characterize graphene on a variety of substrates including, silicon oxide (Koenig et al.,2011) (Boddeti et al., 2013) (Cao et al., 2015), graphite (Wang et al., 2016), and copper (Cao et al., 2014) (Cao et al., 2015). During these tests, a hemispherical cavity is created between graphene and substrate of interest via slow diffusion of gas atoms through the substrate body. After the graphene membrane cavity reaches the desired test volume, the system is placed within an adjustable pressure environment. A negative pressure gradient is applied to the graphene membrane until critical delamination occurs from the substrate (Figure 2.1a). Adhesion energy can be directly calculated from the experiment using a thermodynamic ideal gas model which is a function of membrane geometry dimensions measured by AFM during testing, critical pressure differential at delamination, and material dependent constants (Boddeti et al., 2013).

2.1.2 Beam Fracture Test

Beam fracture experiments involve the creation of a film-stack of interest in a double-cantilever beam (DCB) configuration. This DCB specimen undergoes displacement-controlled Mode I separation, while measuring load, displacement and delamination crack length (Figure 2.1b). Elastic beam theory and linear-elastic-fracture-mechanics are used to calculate adhesion energy which is a function of material properties, layer dimensions, crack length and displacement. A further benefit of this technique is that rate-dependent preferential delamination can be easily explored between different layer stacks. DCB fracture experiments have been used to characterize graphene on silicon (Na et al., 2014), copper (Yoon et al., 2012) (Na et al., 2015), and epoxy (Na et al., 2015).

2.1.3 Nanoindentation

Nanoindentation may be conducted using a variety of tool platforms, including AFM, nanoindenter and interfacial force microscope (IFM) (Section 2.2). During indentation experiments, a probe of known geometry is brought into contact with a substrate of interest and subsequently removed (Figure 2.1c). Both the displacement and force experienced by the probe are recorded by instrumentation during the approach and withdrawal. An appropriate contact mechanics model is then used to calculate adhesion energy between the probe and substrate, which is a function of material properties, probe geometry, and pull-off force. This technique has been used to characterize graphene on silicon (Jiang et al., 2015) (Suk et al., 2016) and copper (Jiang et al., 2015).

A summary of measured adhesion literature values between graphene and various substrates is listed in Table 2.1.

Target Substrate	Measured Adhesion Energy (Jm^{-2})		
	Blister Test	***DCB***	***Nanoindentation***
Silicon	0.45 +/- 4.4% (Koenig 2011) 0.24 +/- n/a (Boddeti 2013) 0.40 +/- 2.2% (Cao 2015)	0.36 +/- 4.5% (Na 2014)	0.46 +/- 5.0% (Jiang 2015) 0.42 +/- n.a. (Suk 2016)
Copper	0.48 +/- 1.4% (Cao 2014) 0.346 +/- 3.2% (Cao 2015)	0.72 +/- 9.7% (Yoon 2012) 6.0 +/- n/a (Na 2015)	0.75 +/- 5.0% (Jiang 2015)
Graphite	0.221 +/- 5.0% (Wang 2016)	-	-

Table 2.1: Reported adhesion energy of graphene on various substrates

2.2 Instrumented Techniques for Interfacial Characterization

Not all surface adhesion experimental techniques are scalable to the development of a commercially available instrumented system. Destructive techniques like blister tests and beam fracture tests are ill-suited to commercial transfer, but nanoindentation is quite the opposite. Over the past decades, numerous platforms employing this approach has been developed, with the most successful being the atomic force microscope (AFM), interfacial force microscope (IFM), and nanoindenter. This section is a critical review of these techniques and provides a more in-depth review of the development of the nanoindenter.

2.2.1 Surface Force Apparatus

Though generally not employed in graphene adhesion studies, the surface force apparatus (SFA) was the first equipment platform designed solely to measure interfacial interactions (Israelachvili et al., 1972). The system was developed such that adhesion

interactions between two coated cross-cylinder-mica sheets could be measured in both air, vacuum, and liquid environments (Figure 2.2a). As the two bodies are brought into near contact, multiple beam interferometry measures the relative displacement of the mica sheets, allowing DMT contact theory to be used to calculate total adhesion energy. The mica sheets can be coated with thin polymer or metal films to observe interfacial interactions between different materials.

A huge advantage of the SFA system is the high tailorability of the stage assembly for different applications (Figure 2.2b). Multiple researchers have reported augmentations to permit high fidelity measurements of specialized surface phenomena including nanorheology (Restagno et al., 2002), weak long range force interactions (Briscoe et al, 2002), and interfaces with simultaneously occurring weak/strong force interactions (Israelachvili et al., 2010). The main drawback of this system is that it is suitable only for measuring interfacial forces over large areas. The size of the mica sheets prohibits closer inspection of smaller interfaces, reducing SFA's utility in graphene characterization.

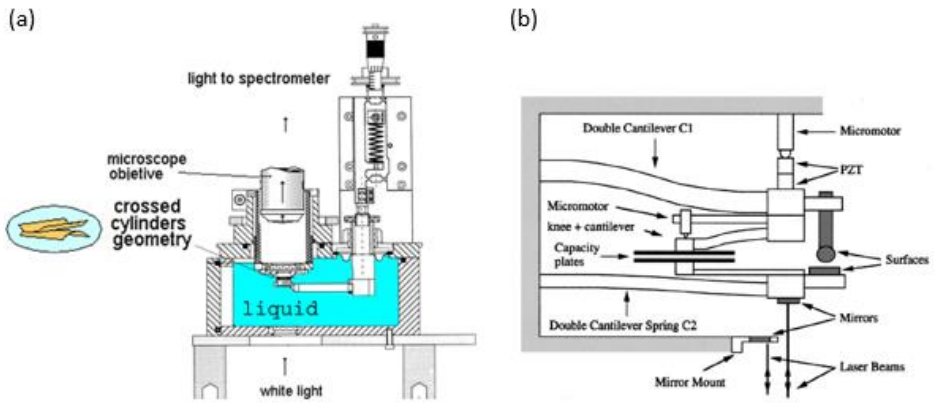

Figure 2.2: (a) Traditional SFA setup with crossed mica sheets (courtesy of UCSB) and (b) modified SFA for capacitive displacement control without mica plates (Restagno et al., 2002)

2.2.2 Atomic Force Microscopy

AFM (Binnig et al., 1986) is perhaps the most popular platform for conducting microscale surface characterization. In typical measurements, a soft cantilever beam with a sharp tip is used to characterize the topography of a substrate of interest. The cantilever beam functions as a spring and responds to surface non-uniformities encountered by the tip with varying degrees of deflection. The cantilever deflection is tracked using a laser-photodetector assembly (Figure 2.3a). The high force resolution of the system (pN) is very attractive for both imaging and interfacial characterization applications.

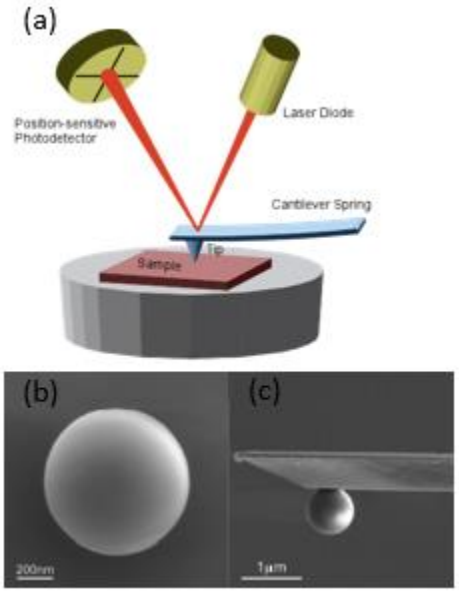

Figure 2.3: (a) Traditional AFM setup (courtesy of Universitat Greifswald), (b) micro-sphere probe and (c) probe-cantilever assembly (Jiang et al., 2015)

For adhesion experiments, the AFM is converted into a nanoindentation device through the mounting of a probe with known geometry onto the cantilever spring (Figure 2.3b-c). Interfacial interactions between the probe and sample surface are measured via cantilever spring deflections. The force and displacement data can then be analyzed using

an appropriate contact mechanics model to calculate adhesion energy and relevant contact characteristics.

The main drawback of this system is measurement "snap behavior" that occurs at close proximity to the surface when the interfacial force gradient surpasses the stiffness of the cantilever beam (Israelachvili, 1991). This snap-to surface behavior is problematic, as it results in an inability to characterize the full adhesion interaction range. Simply increasing cantilever stiffness is not realistic as it is this low compliance which allows the system to achieve pN force resolution. The result of this unstable behavior, is that uncontrolled cantilever setups have reduced applicability for interfacial studies.

2.2.3 Interfacial Force Microscopy

The IFM was developed as a solution to the discontinuous "snap" seen in interfacial experiments using the AFM. This device is essentially an AFM whose cantilever assembly has been modified to accept feed-forward capacitive displacement control (Joyce and Houston, 1991). Implementation of displacement control mitigates the snap instability of the cantilever at high force gradients and permits the instrument to be utilized for high resolution characterization of interfacial interactions (Goertz and Moore, 2010).

The chief drawback of the IFM is that few commercial options exist, so the user must construct their own device. The fabrication of the capacitive plate assembly which functions as both sensor and control scheme is quite complicated with low tolerancing. Device hardware complexity therefore presents a large barrier to entry restricting many research groups.

2.2.4 Nanoindenter

Instrumented indentation (or nanoindenters) are a lesser used method in interfacial research, but they have been slowly garnering attention due to recently improved transducer capabilities that provide sub-nm noise floor and resolution. Like the IFM, commercial nanoindenter systems employ a capacitive plate based transducer that facilitates feed forward displacement control. The primary sensing components (probe, transducer, etc) are rigidly mounted creating a high stiffness loading device with less compliance than traditional cantilever based systems. All these features combine to create a device well-suited for high resolution interfacial characterization of surfaces.

Historically, this technique has not been used for nanoscale adhesion studies but rather microscale characterization of the modulus and hardness of materials. Oliver and Pharr are credited with bringing the technology mainstream by greatly simplifying experimental setup and protocol (Pharr and Oliver, 1992). Their subsequent work developed corrections for common error phenomena, including plasticity and probe profile effects (Pharr and Oliver, 2003). During this period, particular attention was given to modeling the mechanics of indentation with a spherical probe (Field et al., 1994) (Nohava et al, 2011) (Pathak et al., 2015). Spherical probe geometry is frequently utilized in low load indentation applications, where the minimization of contact stresses is desired to allow the analysis of elastic behavior (Field et al., 1994) (Nohava et al., 2011).

During nanoindenter experiments, a spherical probe of known geometry is brought into contact with a target substrate, indented several nanometers into bulk substrate, and then removed. As with AFM and IFM measurements, applied force and relative displacement are recorded throughout the test and contact theory is used to calculate adhesion interactions.

The primary drawback of this platform is that it is fundamentally a quasi-load control device, even when under feed-forward displacement control (Warren et al., 2004). This makes the system susceptible to control instabilities when moving from low to high stiffness regimes, as discovered during our experiments. Methods to mitigate this issue are discussed further in Section 4.2.

Chapter 3: Theory

3.1 Elastic Contact Mechanics

Indentation testing involves a probe of known geometry contacting and penetrating a target substrate to a specified depth, while recording the relative displacement from surface and required force. Depending on the stiffness of the probe, substrate and interaction range there are several contact mechanics theories that are appropriate for modeling their elastic contact. The main differentiator between theories is the degree to which deformation of the probe/substrate is a function of adhesion interactions between the surfaces.

Hertz's theory of elastic deformation was derived in the late 19th century for two spheres in contact. Surfaces are assumed to be smooth, nonconforming and follow linear elastic isotropic behavior. If an equal and opposite load is applied to each sphere, as seen in Figure 3.1, a circular contact zone is produced. The radius a of this contact area can be expressed as a function of load P, effective geometric curvature R, and effective elastic modulus E^*, as seen below.

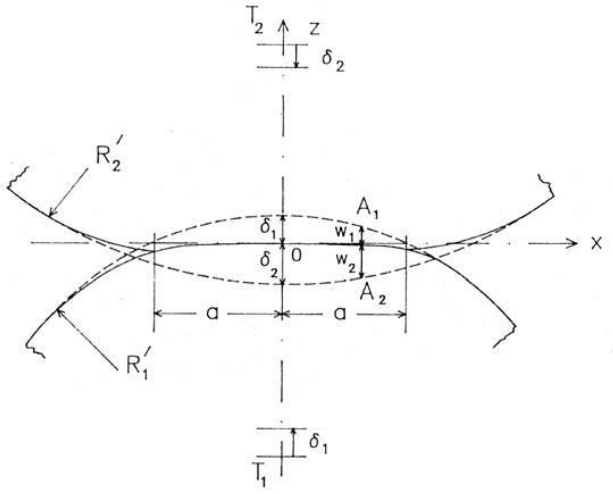

Figure 3.1: General deformation between two neighboring points within solid body (Johnson, 2004)

$$a = \left(\frac{3PR}{4E^*}\right)^{1/3}, \tag{2.1}$$

where R is a function of the radius of curvature for each body

$$\frac{1}{R} = \frac{1}{R_1} + \frac{1}{R_2}$$

and E^* is the ratio of the elastic properties for each body

$$\frac{1}{E^*} = \frac{1 - v_1^2}{E_1} + \frac{1 - v_2^2}{E_2}.$$

As the applied force P increases and bodies undergo compressive deformation, the relative displacement δ of a surface point can be described by

$$\delta = \left(\frac{9}{16}\frac{P^2}{E^{*2}R}\right)^{1/3} \tag{2.2}$$

This force-displacement model assumes a constant contact pressure distribution and neglects adhesion interactions between the two bodies. Hertzian contact mechanics works well for macro loading domains but requires refinement for situations involving bodies in low load contact. During low load contact, adhesion phenomena produce surfaces forces whose influence on contact radius and displacement cannot be neglected (Tabor et al., 1969).

Using an elasticity and energy analysis, Johnson-Kendall-Roberts published an amended Hertzian contact radius solution to account for body surface energy γ (Johnson et al., 1971).

$$a = \left(\frac{R}{E^*}\left(P + 3\gamma\pi R + \sqrt{6\gamma\pi RP + (3\gamma\pi R)^2}\right)\right)^{1/3} \tag{2.3}$$

where the effective surface energy γ is a function of the surface energy of each body and their interaction through

$$\gamma = \gamma_1 + \gamma_2 + \gamma_{12}. \tag{2.4}$$

The JKR solution yields a parabolic distribution of compressive stresses transitioning to tensile loads near the edge of the contact area. This behavior is founded on the assumption that surface forces act significantly only within the region of contact. Adhesion interactions are assumed to be negligible in the non-contact area surrounding the region of contact between bodies. These assumptions work well for compliant bodies, but as stiffness increases, deviation from predicted behavior occurs.

Derjaguin-Mueller-Toporov used a similar analytical approach to JKR, but included non-contact surface adhesion interactions in their problem setup (Derjaguin et al., 1975). The final contact area solution is very similar to Hertz's original formulation, but modifies the input load to include the contribution from surface forces.

$$a = \left(\frac{R}{E^*}(P + 2\pi\gamma R)\right)^{1/3} \tag{2.5}$$

This modification results in Hertzian stress behavior within the contact zone and tensile stresses in the noncontact region. These tensile loads are maximum immediately outside the contact zone and parabolically decay as a function of distance.

Equilibrium separation corresponds to the contact area present between two bodies at zero load. An applied tensile load is required to completely separate the bodies and the maximum value of load occurring at separation is termed the *pull-off force.* This

pull-off force can be analytically determined from Eq 2.3-2.5 by setting the contact area to zero and solving for the load. The JKR and DMT models predict different maximum pull-off forces which may be seen below.

$$P_{JKR} = \frac{3}{2}\pi\gamma R \tag{2.6}$$

$$P_{DMT} = 2\pi\gamma R \tag{2.7}$$

The non-dimensional Tabor parameter may be used to ascertain whether the JKR or DMT model is more appropriate for a contact scenario (Tabor, 1977). This parameter is the ratio of contact region neck height to equilibrium inter-atomic bond distances between bodies:

$$\mu = \frac{h}{Z_0} = \left(\frac{\gamma^2 R}{E^{*2} Z_0{}^3}\right)^{1/3}, \tag{2.8}$$

where contact neck height may be calculated using Hertzian mechanics

$$h \cong \left(\frac{R\gamma^2}{E^{*2}}\right)^{1/2}.$$

For small values of μ, where μ<<1, DMT is the most appropriate contact model. Scenarios producing small μ are bodies with high stiffness, small radii of curvature, or very low adhesion interactions. For large values of μ, where μ>>1, JKR is the advised method. This corresponds to compliant bodies, large radii of curvature, or high adhesion interactions.

Chapter 4: Experimental Technique

4.1 Overview

All adhesion measurements were conducted using a Hysitron TI-950 system with an xProbe MEMs type transducer. This transducer has a sub-nanometer displacement noise floor permitting ultra-low load tests to be conducted with 0.04 nm displacement resolution. Test specimens are epoxy mounted on magnetic steel AFM sample disks and placed in the insulated stage chamber. Figure 4.1 illustrates a typical test setup with transducer assembly and mounted samples clearly visible.

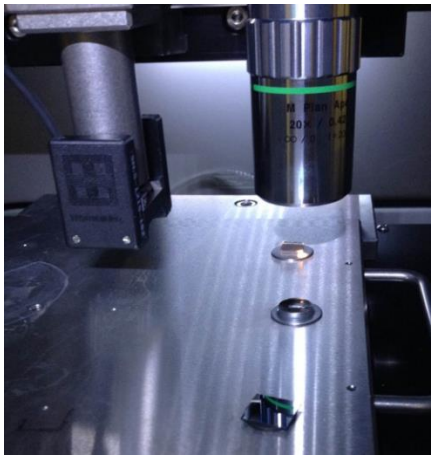

Figure 4.1: Typical nanoindentation test setup

All tests were implemented from imaging mode using a custom-tuned displacement control function. In imaging mode, the probe is brought into contact with the target substrate using a combination of coarse and fine z control. The system is left to stabilize over a several-hour period and then all tests are conducted from the surface start point. This technique greatly minimizes thermal error present in measured data.

The experimental displacement function can be seen in Figure 4.2. The function specifies (1) an initial 40 nm pullback from the surface, (2) a subsequent 40 nm re-

approach and (3) 5 nm indent, followed by a (4) final 40 nm re-withdrawal from the surface. Note that surface contact occurs at a relative displacement of zero. Force-displacement data from segments (2) and (4) were analyzed to characterize the adhesion interactions between the diamond probe and target substrate. The data from segment (3) was used to validate the test using Hertzian contact mechanics.

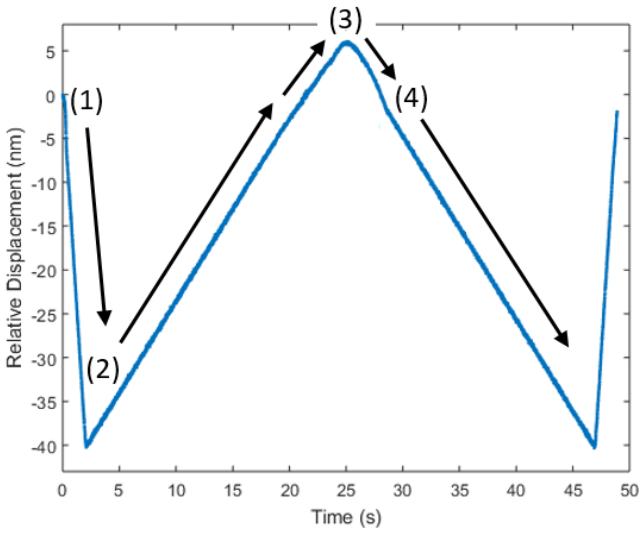

Figure 4.2: Experimental displacement function

4.2 Motor Control

During data collection, the nanoindenter system locks all electromechanical actuators and the transducer performs the required actuation to create the load-displacement curve. Historically, there have been three options for controlling transducer actuation: open-loop control, load control, and displacement control. All methods have associated benefits and drawbacks which will be discussed in the following paragraphs. Over the course of our investigation, all methods were attempted and ultimately displacement control was selected due to its resistance to "snap" responses in the adhesion zone.

4.2.1 Open-Loop Control

Open-loop control is voltage load control. Through preliminary open-loop testing, the displacement response of the material to given loads is characterized. A target peak displacement and corresponding load is selected and this target peak load is set in the software. This load corresponds to a given voltage, so the software will discretize the total load range from zero to peak load into incrementally increasing voltage segments. The voltage-load resolution is a function of the total time of each load segment. As total time increases, voltage discretization increases along with resolution.

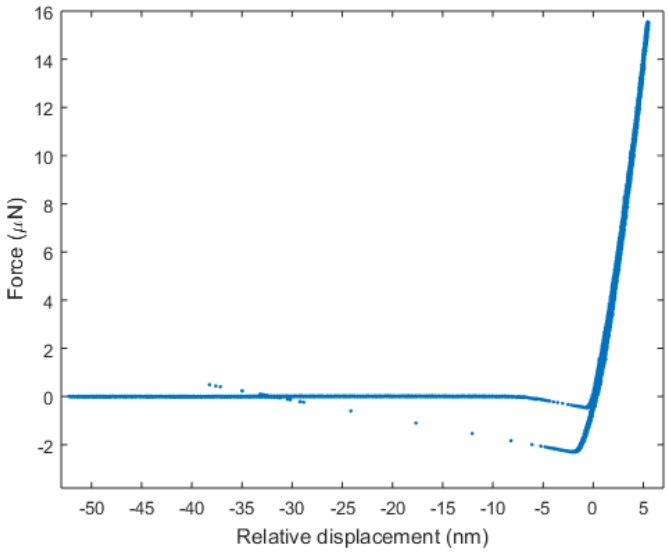

Figure 4.3: Open-loop "snap" response on HOPG graphite

Open-loop has no feed forward control which results in higher susceptibility to adhesion zone "snap" behavior. This unstable behavior can only be partially mitigated through increasing voltage discretization and increasing data collection rates. During test optimization, we found that instability could only be removed from the approach data.

Withdrawal data always exhibited “snap-from” behavior that resulted in false interaction range as seen in Figure 4.3.

4.2.2 Load Control

Load control is a simplified PID controller and fairly straightforward to setup. As with open-loop control, preliminary characterization of material displacement response to given loads must be completed. Then once a target load has been selected, the integral gain is adjusted until the system follows the load path during testing. All other PID tune parameters are locked out within the software, so there is essentially only one knob to adjust for load control.

Displacement controlled measurements are the gold standard of interfacial research, so device load control was not developed over the course of this work.

4.2.3 Displacement Control

Displacement control is a conventional proportional-integral-derivative (PID) feedback loop. The integral gain setting is the principal feedback element governing adherence to desired path behavior. Proportional and derivative settings are used to reduce instabilities occurring during path transitions. As most nanoindenter systems are quasi-load-control devices, the performance of displacement control is typically lower than load control and more difficult to achieve through appropriate PID gain tuning.

The implementation of displacement control is very different from the previously described control regimes, as no preliminary material response characterization is required. A target displacement is selected and then the PID gains are individually adjusted until the desired displacement path is followed during testing. This is an experimentally iterative process.

During the course of experimental setup, we found that both probe-tip velocity and changing negative stiffness in the noncontact adhesion zone had a huge impact on the tuning process, specifically in contributing to a phenomenon called transducer "ringing." This phenomenon is a byproduct of excessive energy input into the transducer control system through elevated gain settings. As seen in Figure 4.4, "ringing" is characterized by the onset of instability within the displacement control loop and uncontrolled oscillatory behavior. During these uncontrolled oscillations, the transducer displacement can wildly fluctuate by tens of nanometers until the control loop re-stabilizes. The onset of ringing always occurs at the adhesion region transition zones and is a result of the rapid transition from zero stiffness to negative stiffness (approach) or vice versa (withdrawal).

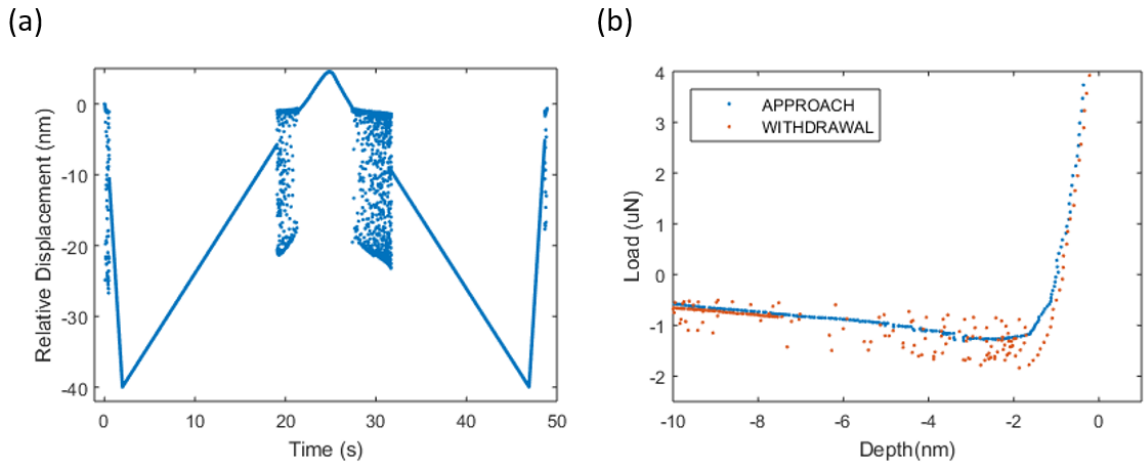

Figure 4.4: (a) Transducer ringing near onset of adhesion region and (b) ringing impact on withdrawal force-displacement data

Through experimental characterization, it was found that a combined reduction of probe-tip test velocity and integral gain could remove all ringing (Figure 4.5). The system control settings could be tuned on a golden reference sample and then the same settings

could be applied to all test samples. All measurement data presented in Section 5 was obtained by initially tuning the system on fused silica as the gold standard.

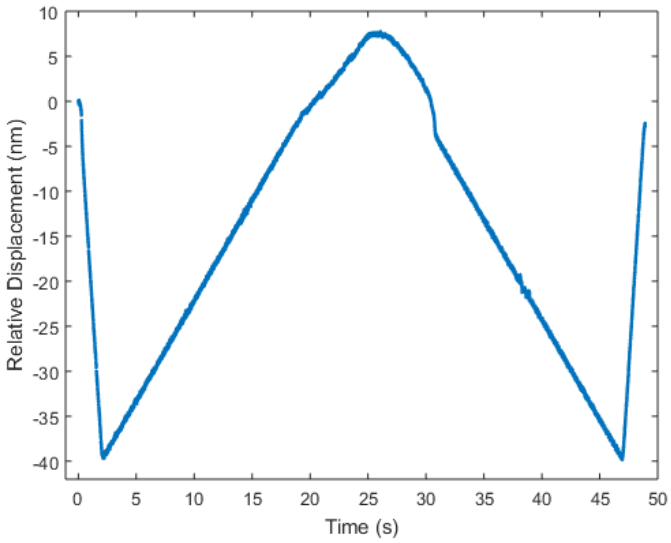

Figure 4.5: Optimized displacement function to remove "ringing"

4.3 Error Mitigation

Sources of error in nanoindentation have been well characterized over the past decade, a fact which is increasingly reflected in equipment design. Current systems are typically thermally and acoustically isolated from their environment, lowering overall noise floors and increasing sensitivity. For our investigation, further development of error mitigation techniques was required to maintain a DMT validation error rate of less than 10%. These techniques were developed to reduce thermal, equipment hardware, and testing error are discussed in the following paragraphs.

4.3.1 Thermal Error

Thermal drift is a serious concern for nanoscale testing and causes false force-displacement data when present. Thermal error is typically the result of the sample or

indenter assembly expanding/contracting with minute temperature fluctuations, causing ranging displacement values (Fisher-Cripps, 2006). The TI-950 has a multitude of built-in hardware and software solutions to mitigate impact of thermal drift, which were then coupled with specialized testing protocols to further reduce the prevalence of error. Typical drift rates for our indentation tests were ~0.03 nm/s and were achieved through the following mitigation techniques.

External thermal instability was minimized through the utilization of a temperature controlled testing room and an insulated instrument enclosure. Internally, the main thermal sources are the DC motors controlling the XYZ stage. To mitigate motor thermal impact, all testing was completed using Imaging Mode coupled with a stabilization period. This inactive period allowed the motors and chamber to reach thermal equilibrium prior to testing.

The Triboscan software on the instrument contains a thermal drift correction routine that automatically runs prior to data collection. While in contact, total transducer displacement drift (nm) is measured over a set window and used to calculate a rolling drift rate average (nm/s). Once the drift rate is considered “stable”, the indentation test is initiated. A linear offset is then applied to the final force-displacement dataset to correct for the calculated drift rate. Following iterative empirical testing, a total period window of 90 seconds and a rolling average timeframe of 20s were selected to encourage drift stability.

4.3.2 System Error – Initial Penetration

Initial penetration error is an artifact of how the system defines the initial contact point with the substrate. A “pre-load” is set previous to testing, designating the minimum load level that is considered initial contact. As the probe-tip searches for the surface, the system will “zero” the contact depth once the preload level is observed. This pre-load value inherently causes some level of elastic deformation, so there is always a margin of error with the system “zero” and actual zero.

This magnitude of error was qualified through a pre-load study using a 10um conical probe mounted on the standard 1D Hysitron transducer. All testing was conducted on a fused-quartz calibration sample to a fixed depth, while varying the pre-load magnitude. Figure 4.6 shows that as preload is increased from 0.2uN to 8uN (noise floor of standard transducer), we see that the force-displacement curve steadily shifts towards the left. This shift is directly proportional to the level of displacement error within the measurement, as the machine “zero” now includes increasing elastic deformation. Additionally, as pre-load decreases, the magnitude of shift continually decreases until a baseline preload, after which no improvement is registered. For our data, this convergence occurs at a pre-load of 0.5 μN.

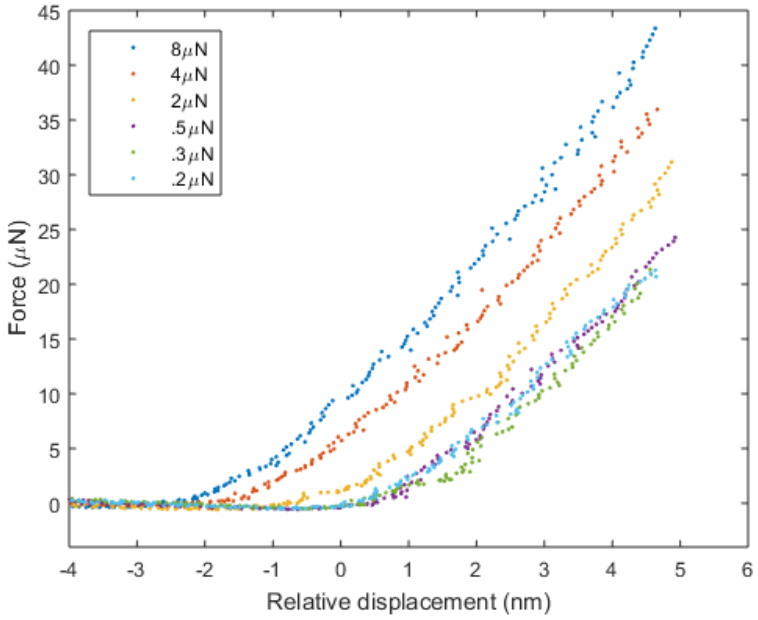

Figure 4.6: Initial penetration dependence on machine preload setting

The key takeaway of this study is that initial penetration error continually decreases as pre-load is reduced up until a certain minimum value. After this optimal pre-load value, there is no further error reduction as seen in the force-displacement offset. As pre-load is decreased past this optimal value and approaches the noise floor, the possibility of "false engages" increases. Therefore, this optimal pre-load value was used for all subsequent testing. For our MEMs type xProbe transducer, we used a pre-load value of 50 nN.

4.3.3 System Error – Displacement Control

Following the successful setup of displacement control in our experimental technique, we discovered that there were persistent repeatability and accuracy issues in our force-displacement data. After further testing, we realized that the root cause of these issues was not hardware error but an inconsistent zeroing of the x-y axis of the force-

displacement data. The final solutions described in the proceeding section are reliable methods to zero both the force and displacement axes of the indentation dataset.

The first issue addressed was a linear force ramp phenomenon present in the non-contact data during withdrawal from the substrate surface. Depicted in Figure 4.7, this linear drift was consistently present on all withdrawal stages and was highly repeatable in magnitude. This is an accuracy issue as the transducer is expected to register zero load at large distances from the substrate surface.

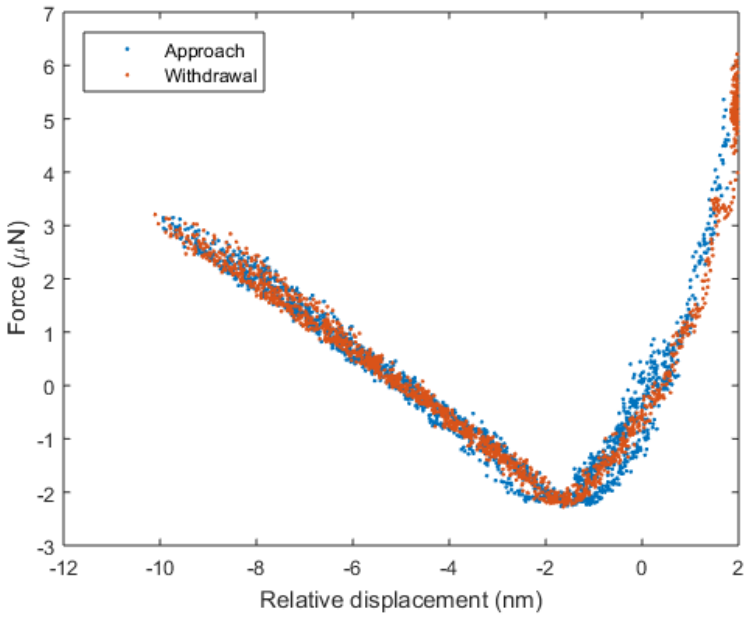

Figure 4.7: Linear force ramp phenomenon on both approach and withdrawal

Suk (Suk et al., 2016) encountered a similar issue during nanoindentation testing and employed a linear fit to perform a global offset on the dataset. The underlying assumption permitting this offset is that if the probe tip is removed sufficient distance from the substrate, noncontact force interactions with tip are minimized. Caution needs to be employed when selecting the minimum distance at which zero interactions begin, as

longer range interactions can be generated from water bridging and tangling debris. After consultation with Hysitron application engineering, Suk selected -20 nm to -50 nm as the displacement range on which to employ a linear fit and use as an offset basis (Suk et al., 2016).

This same linear regression technique was successfully employed as a solution to our force ramp. The regression slope was calculated for each dataset between -20 nm to -50 nm and was applied as a global offset. An example of this technique may be seen in Figure 4.8 below. This particular dataset has been shorted, so the global offset has been applied using a linear fit from -10 nm to -5nm. Nonetheless, using this global offset technique, a ramp-free dataset is generated as seen in Figure 4.8. This technique effectively performs a vertical offset on the data and sets the force data to zero outside the interaction range.

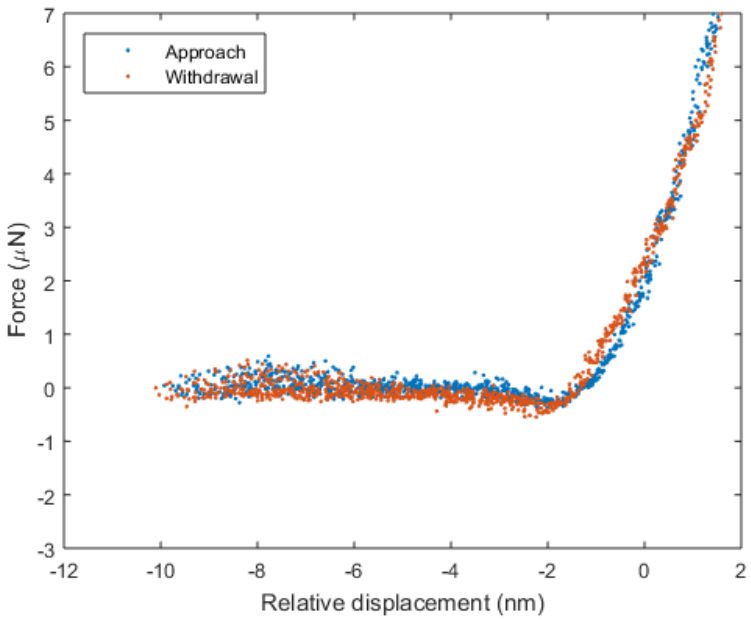

Figure 4.8: Linear offset removes ramp behavior during approach and withdrawal

The second issue that was resolved was inconsistent zeroing of the displacement data by the system during testing. The root cause of this inconsistency is unknown as the pre-load value had been optimized to minimize penetration error. Figure 4.9 shows a typical example of inconsistent force-displacement data measured using identical displacement control PID settings. These five tests were performed sequentially at the same location using the fused-silica calibration sample, while varying the peak displacement. The measured force-displacement elastic response of a single specimen should not vary as a function of test order, which is clearly seen below.

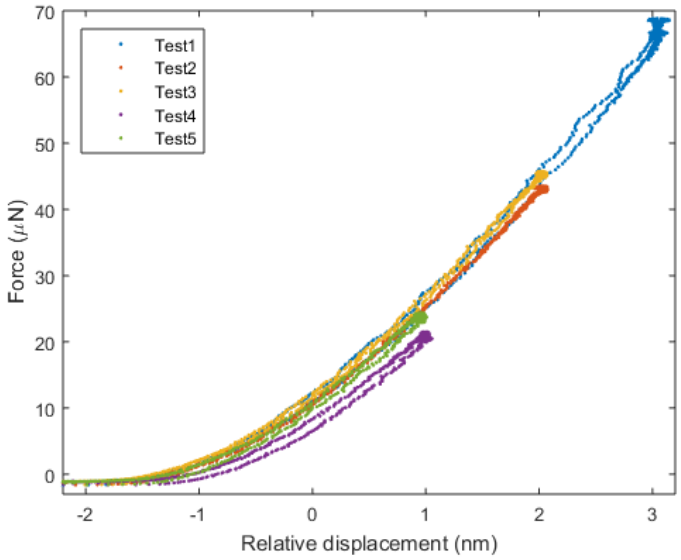

Figure 4.9: Inconsistent response measured on quartz sample

To rectify this unwanted variation, we employed a global offset using the assumption that at zero applied force, there should be zero displacement. Once the force axis had been zeroed to remove the force ramp issue, we could be reasonably sure of the correct location of zero force. The displacement axis was then shifted so zero

displacement corresponded with zero force. This method was extremely successful in removing all repeatability issues.

Figure 4.10 presents the same quartz dataset from Figure 4.9, but all force-displacement responses have been offset using the previous zero force assumption. All measured responses now have overlapping load/unload segments, as would be expected in elastic loading situations.

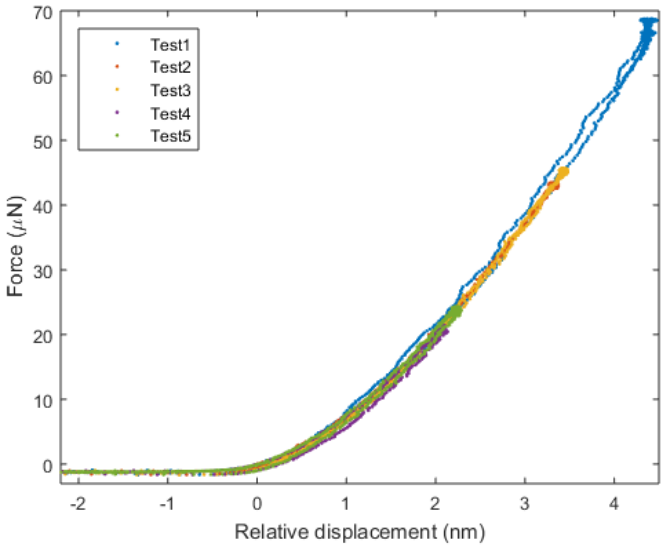

Figure 4.10: Offset corrected quartz data

The effectiveness of this offset approach was also verified on inconsistent force-displacement behavior produced by varying PID displacement control settings. Figure 4.11 illustrates typical system measurement behavior when PID setting magnitudes are increased across sequential tests.

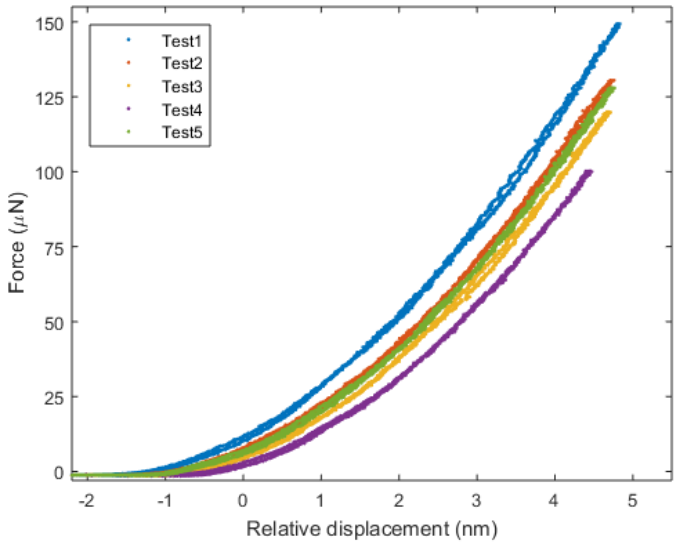

Figure 4.11: Variable response measured on quartz resulting from PID control changes

The artificial spreading behavior present in Figure 4.11 can be completely corrected by employing the same displacement offset technique. The offset corrected dataset can be seen Figure 4.12 below.

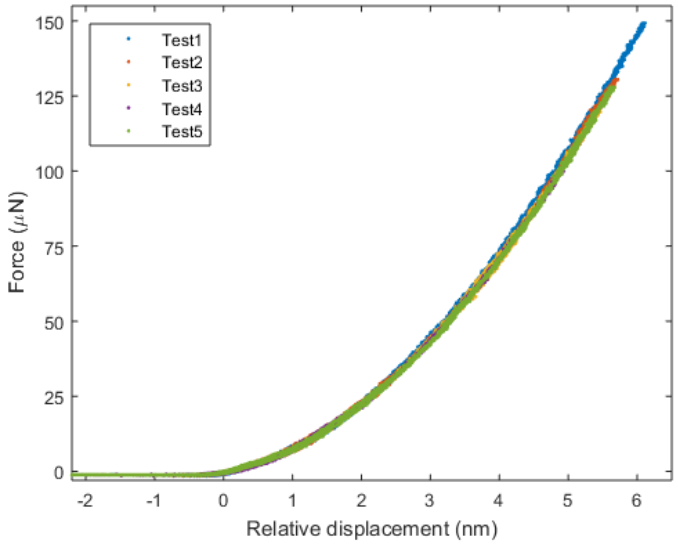

Figure 4.12: Offset corrected quartz variable PID control data

4.3.4 Hardware Error – Probe Surface Condition

Error introduction through probe contamination is a serious concern for adhesion measurements and was a reoccurring issue throughout testing (Figure 4.12). Debris can have a major impact on the probe curvature, as well as complicate the effective stiffness of both bodies. Collectively, uncertainty in both parameters introduces substantial error in both our DMT adhesion model and Hertzian contact validation model.

The ability to remove foreign contamination is perhaps the greatest weakness of the MEMs-type transducer. As the probe is rigidly attached to the transducer, manual cleaning is impossible. The only recourse is to utilize the piezo-raster feature of the system in attempt to remove contaminants via friction or surface attraction. Through collaboration with Hysitron, we implemented a platinum sample cleaning method to remove carbon and other foreign debris. However, the experimental application of this method yielded marginal results (Figure 4.12a shows tip after platinum raster).

The only effective method observed to clean MEMs-type probes is a focused ion beam (FIB) clean. The probe shown in Figure 4.12a was returned to Hysitron for FIB cleaning and was successfully returned to an “as new” condition (Figure 4.12b).

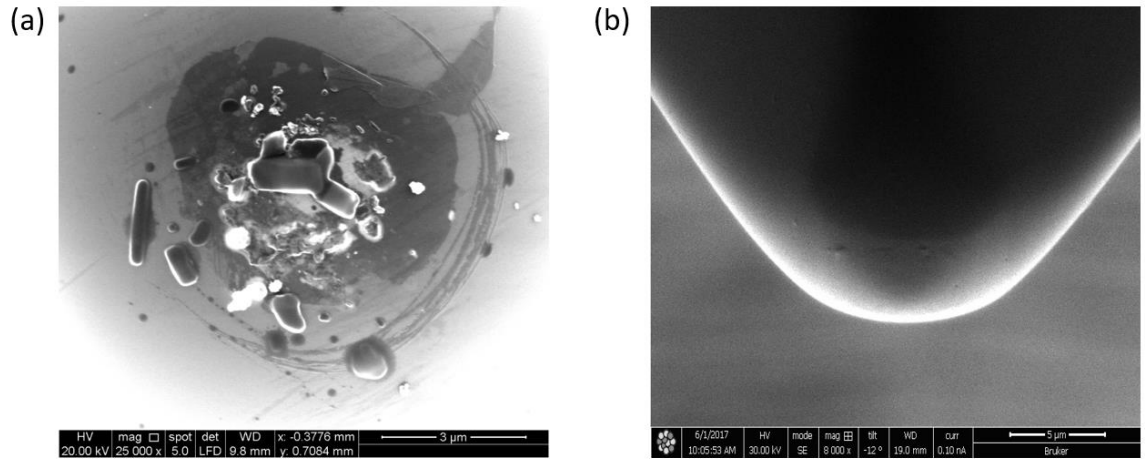

Figure 4.12: (a) SEM image of probe covered in particular contaminants and (b) contaminant-free probe following FIB clean

Chapter 5: Results

5.1 Overview

The test protocol developed over the course of our investigation relied heavily on the previous published work of Suk and collaboration with the engineering expertise at Hysitron (Suk et al., 2016). Suk performed similar adhesion measurements on silicon, graphite, and graphene-silicon samples, but used a conical tip with a radius three orders of magnitude smaller (~50 nm). By significantly increasing our test probe size, we hoped to amplify the adhesion zone forces, thus increasing the sensitivity of our test. To this end we were quite successful, our measured adhesion forces on silicon and graphite were two orders of magnitude larger than reported by Suk. A comparison of measured vs. literature graphite response can be seen in Figure 5.1. The peak adhesion force experienced during approach occurs around 2 nm relative displacement and is ~500 nN vs 10 nN. Additionally, the signal to noise ratio of our dataset shows great improvement vs. Suk's data.

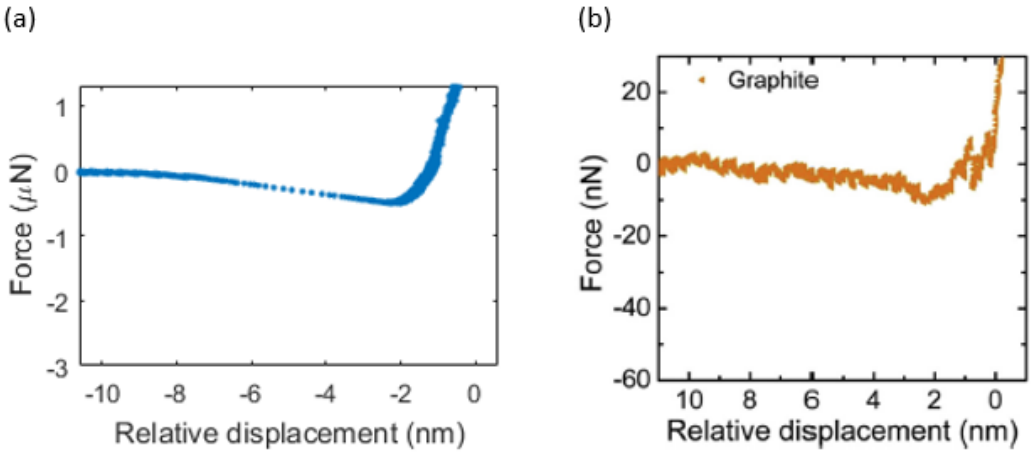

Figure 5.1: (a) Measured graphite adhesion response on approach and (b) literature graphite response on approach (Suk et. al., 2016).

However, an unseen consequence of amplifying adhesion forces were complications in the displacement control PID setup. Increasing adhesion forces seen at the probe-tip created a stronger transition "shock" at the boundary between the non-contact approach, withdrawal segments and adhesion zone. This shock encouraged non-optimal behavior (i.e. noise and "snap"), which had to be mitigated through a combination of PID tuning and probe velocity adjustment.

The finalized measurement protocol was used to successfully characterize tip interactions on fused-silica and graphite. Unfortunately, the reliability of further MEMs-type transducer experiments was compromised due to the accumulation of tip debris. Our group switched to the standard transducer (non-MEMs) and characterized interfacial interactions on a silicon substrate. Results from both transducers matched existing results in the literature on silicon and graphite and measured load-displacement behavior generally displayed good agreement with DMT contact models (except on graphite).

5.2 FUSED-SILICA

Fused-silica (or quartz) is the standard reference sample for nanoindentation due to stable and isotropic bulk behavior, so naturally appeared to be an excellent starting point for developing an adhesion measurement protocol. Unfortunately, this assumption was found to false over the course of experimentation, as long-term quartz surface characteristics are not repeatable. Quartz is hydrophilic, so the top surface layer behaves much like glass and is permeable to water for the top several nanometers. Variable humidity conditions therefore lead to changing interfacial interactions, a result of changing water composition of quartz's surface layer.

There is a distinct lack of literature values for adhesive interactions between quartz and diamond probes, so collaboration with Hysitron was necessary to attempt the

creation of an adhesion energy baseline reference. Mirrored experiments were carried out at the Hysitron corporate facility in Minnesota and at UT-Austin, using identical test protocol, equipment, and environment conditions. Relative humidity (RH) conditions were matched within 5% (nominal RH~ 55%) and the MEMs-type transducer was used with a 10 µm radius conical probe. Further Hysitron testing on quartz was then completed at a later date using a reduced tip size (R=50 nm). Results from these experimental studies may be seen in Figure 5.2.

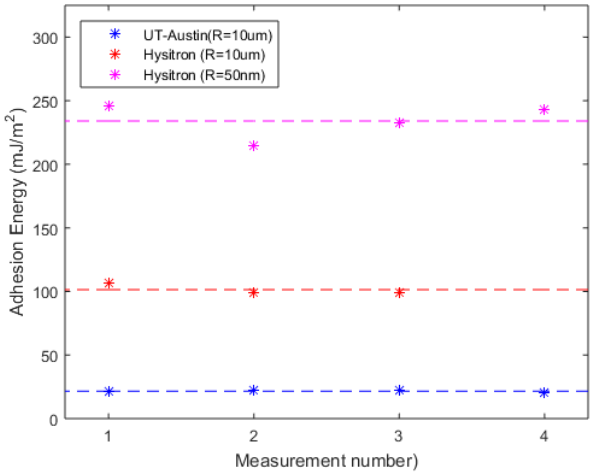

Figure 5.2: Compiled quartz adhesion results across experiments

The compiled quartz adhesion results exhibit large variation across datasets suggesting that quartz is not an ideal choice for adhesion calibration. This lack of repeatability even in humidity-matched studies, suggests that surface water content is not the sole variable responsible changing adhesion interactions. Our suspicion, is that varying probe surface or sample conditions are the primary contributors to this discrepancy, as contaminant debris could potentially account for such a large data range. However, though there is strong variance between experiments, the repeatability within

datasets is excellent. The coefficient of variance within all three datasets is less than 5%, suggesting that the metrology platform and experimental protocol are stable.

5.3 GRAPHITE

The interfacial interactions between graphite and various materials has long been of interest to the scientific community due to graphite being the precursor to exfoliated graphene. Literature data on the adhesion response between graphite and a diamond indenter for ambient conditions was published previously by Suk (Suk et al., 2016). By mirroring equipment platforms, the expectation was that measured behavior should agree well with Suk and his group.

Unfortunately, the MEMs-probe contamination issue immediately arose following our period of graphite testing, calling into question the accuracy of the majority of collected data. The only probe area calibration during this period was performed near the end of testing (before Test2) and showed an increase in probe radius of 45%. Whether this was an incremental process or sudden occurrence is unknown, but this uncertainty forced the removal of all data except for two rounds of tests which occurred around the time of area calibration.

Typical measurement interaction ranges deviated from those observed by Suk and demonstrated clear “snap to” behavior (Figure 5.3). This behavior was likely the result of the 50% probe curvature enlargement, which led to decreased stability in our displacement control. The sudden snap on approach masks a significant portion of tip-graphite interactions, but it is clear that the bodies begin interacting around 6 nm with maximum force occurring at 2 nm. This is slightly different from Suk, who observed an earlier initiation of interactions but identical displacement corresponding to maximum force.

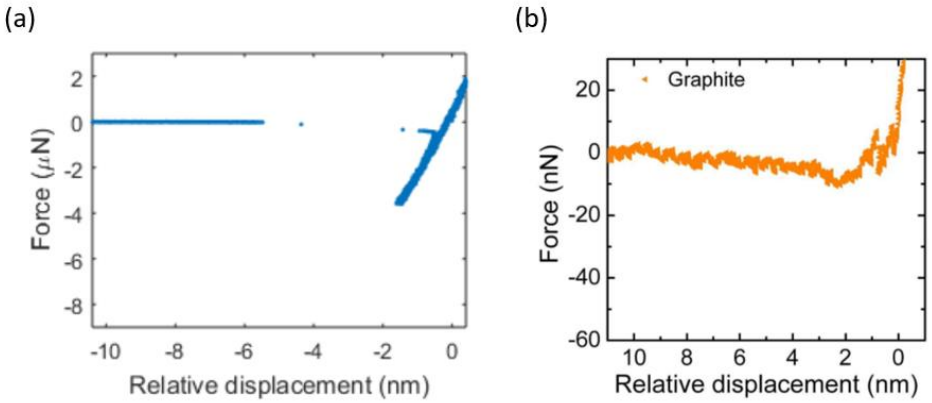

Figure 5.3: (a) Measured graphite adhesion behavior and (b) literaure behavior (Suk et al., 2016)

The peak adhesion energy on approach for experimental and literature data can be seen in Figure 5.4. There were insufficient tests per dataset to truly comment on within test repeatability, but there is a large variation in test-to-test averages, with a relative discrepancy of 47%. This variation could be due to nonuniform environmental conditions between tests (there was a three-week gap between Test1 and Test2) or incorrect assumption of the radius of curvature for Test1. The average between both tests is depicted as the blue dashed line, which has a 18% relative error when compared with the literature average. However, Test2 has an accurate area calibration and is within 5% of the literature average, suggesting that the true root cause for variation is uncertainty in the radius of curvature for Test 1.

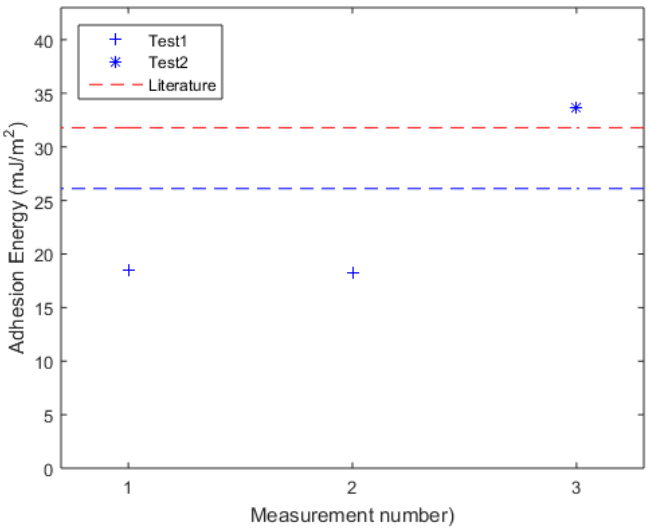

Figure 5.4: Measured graphite adhesion response vs. literature

5.4 SILICON

Single-crystalline silicon is anisotropic with varying directional mechanical properties according to crystallographic orientation. Of the possible lattice orientations, silicon (111) is the most useful for indentation due to transverse isotropic properties. Following the contamination of our MEMs-transducer assembly, a standard Hysitron transducer was selected for continued testing. This hardware switch had the benefit of allowing the validation of our experimental protocol on a less sensitive device.

The standard transducer was utilized with a 10 µm conical probe to investigate the ambient adhesion response on bare silicon (111). This same experiment was conducted by Suk using a MEMs-transducer, allowing comparison with published literature results (Suk et al., 2016). Similar to graphite, measured length of interaction on approach deviated from that observed by Suk (Figure 5.5). However, the disparity in behavior from -6 nm to -2 nm is fairly significant, indicating that there is a much stronger short-range

attractive force operating in Suk's work. The source of this force is unknown but could be due to sample surface composition variation

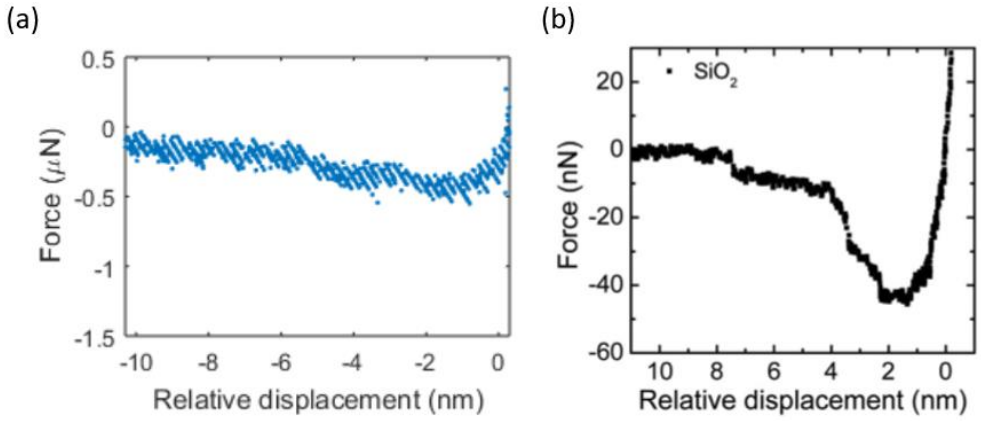

Figure 5.5: (a) Measured silicon adhesion behavior (ambient) and (b) literature behavior (Suk et al., 2016)

The peak adhesion energy on approach for experimental and literature data can be seen in Figure 5.6. Experimental data and literature values agree well and there is a 4% difference between the two dataset averages (dashed lines). There is a 7% coefficient of variation for the experimental dataset, which is reasonable when accounting for site-to-site variability.

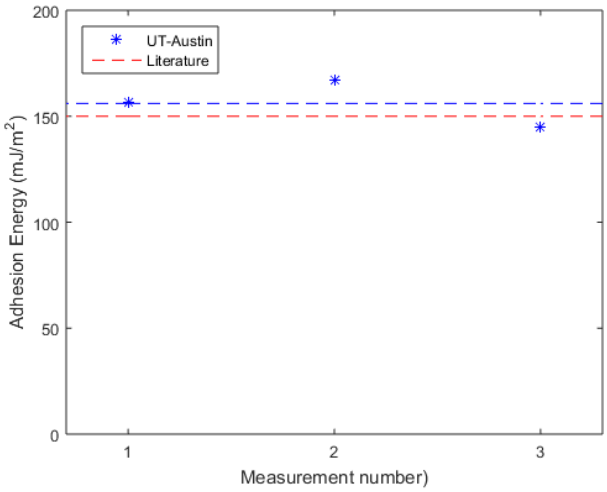

Figure 5.6: Measured ambient silicon adhesion response vs. literature

Following the return of the refurbished MEMs-transducer and probe assembly (now certified contaminant free, Figure 4.12b), further testing was performed on Si (111) in a nitrogen environment. Prior to indentation, nitrogen was introduced into the testing chamber until measured chamber relative humidity decreased to RH=13%. This RH value corresponds to reported experimental setup of Suk's nitrogen-mix environment and allows direct comparison with literature data (Suk et. al., 2016).

Consistent snap-to behavior on approach and withdrawal lead to an inability to resolve the measured length of interaction past 4 nm. Proceeding up to 4 nm, there is little to no adhesion interaction between the two surfaces (Figure 5.7a), which is similar to Suk's findings where interactions began around 5 nm (Figure 5.7b). Once adhesion interactions initiate, we are unable to record any of the further detail that Suk measured due to the performance of our motor control.

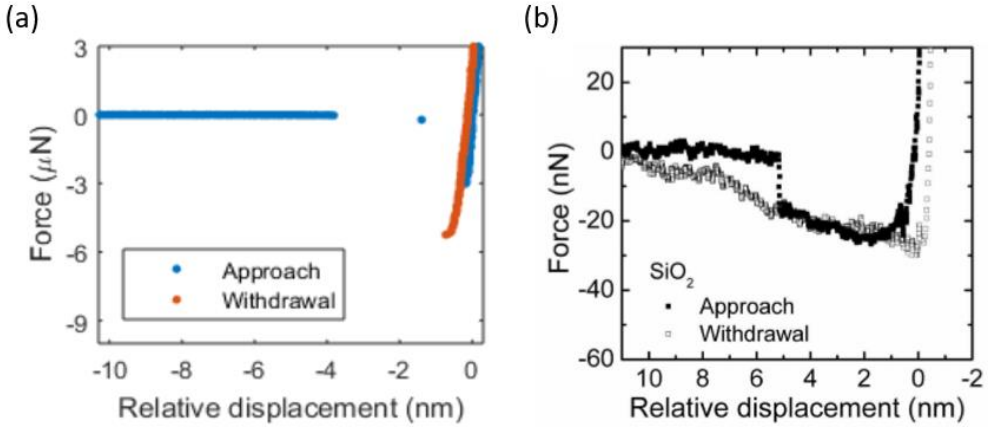

Figure 5.7: (a) Measured silicon adhesion behavior (nitrogen mix) and (b) literature behavior (Suk et al., 2016)

The peak adhesion energy on withdrawal for experimental and literature data can be seen in Figure 5.8. As in ambient test conditions, experimental data and literature values agree well and there is a 2% difference between the two dataset averages (dashed lines). There is a 15% coefficient of variation for the experimental dataset, which is larger than expected but clearly brackets the literature value. During testing, site location was changed following every two measurements which contributed to the bimodal behavior above. As discussed previously, site adhesion characteristics routinely vary, but within site repeatability remains high.

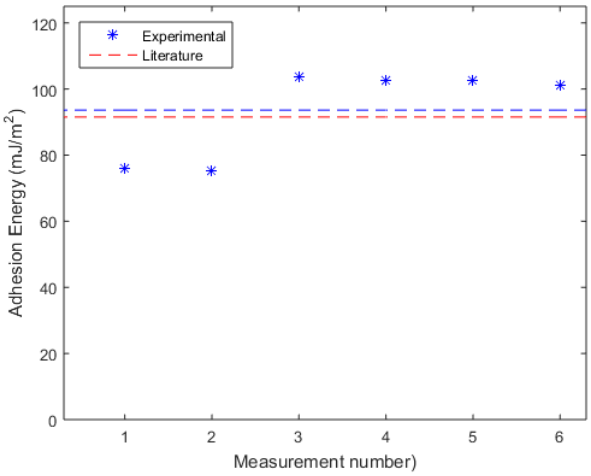

Figure 5.8: Measured nitrogen-mix silicon adhesion response vs. literature

Chapter 6: Summary and Future Work

6.1 Thesis Summary

The successful implementation of a dry R2R graphene transfer process has the potential to revolutionize the consumer electronics industry and usher in an era of flexible device ubiquity. Integral to this future success, is continuing research into the interfacial characterization of graphene on key substrates. This research vein is comprised of numerous methods and instrumented platforms, all with varying strengths and weaknesses depending on application space. For nanoscale interfacial experiments, displacement-controlled nanoindentation has continually proven to be the most adept at measuring adhesion strength with the highest resolution of displacement interaction range.

Though there are several instrumented platforms utilized for displacement-controlled nanoindentation, AFM-based experiments are generally the most prevalent in literature. Recently, a team of researchers published interfacial results characterizing single and multilayer graphene on silicon substrate using displacement-controlled nanoindentation via nanoindenter (Suk et. al., 2015). The work reported here followed on Suk's success by implementing a displacement-control measurement protocol on UT-Austin's Hysitron ATI-950 nanoindenter.

Over the course of this study, our protocol was used to measure the adhesive interactions between the diamond probe tip on quartz, graphite and silicon samples. Of these three samples, comparable literature nanoindentation data existed only for silicon (111). Our experimentally calculated adhesion strength between probe tip and silicon (111) sample (in both ambient and nitrogen environments) correspond well to Suk's data. For both environments, there is less than 5% relative discrepancy between our experimental adhesion strength average on withdrawal and that of literature (Suk et. al.,

2015). The coefficient of variation (COV) for our ambient and nitrogen environment experimental data is 7% and 15%, respectively. The increased COV for our nitrogen environment data can be attributed to site-dependent variability, a commonly occurring phenomenon in adhesion experiments.

Though successful in measuring adhesion strength, our experimental platform failed in measuring adhesion interaction ranges to the expected level of fidelity. Consistent snap-behavior on both approach and withdrawal reduced our expected displacement resolution from 0.4 nm to 5 nm-10 nm. This resolution reduction was due to the inability of our displacement motor control tune to adequately compensate for the sudden stiffness transition upon entering the adhesion interaction region. Suk encountered no serious displacement control issues as his probe geometry was evidently sufficiently small to reduce transition shock at the adhesion zone interface. This indicates that there exists a range of probe radii for which the instrument can make high fidelity measurements, but our 10 μm radius probe is clearly outside this utility region.

Another key finding of this work focused on appropriate reference samples for calibrating surface adhesion measurements. Experiments indicate that silicon (111) is the ideal calibration standard for the probe tip, which is a departure from the typical industry standard of fused quartz. Our experimental data clearly showed that though the bulk behavior of quartz is stable, quartz's surface characteristics are highly variable. This variability is a product of quartz's permeability to moisture for the initial surface layers and decreases past 10 nm.

In conclusion, though the nanoindenter platform offers high theoretical displacement resolution for characterizing interaction range, this performance is strongly dependent on probe radius. The root cause of this dependency is that the platform is fundamentally a quasi-load control device. For larger probe radii, encountered adhesion

forces at the transition region overwhelm the capabilities of the system displacement motor control. This platform is entirely capable of measuring adhesion strength, but another platform should be selected if high resolution measurements of interaction range is desired.

List of the main contributions presented in this report:

1. Developed measurement protocol with error mitigation techniques for adhesion measurements using Hysitron ATI-950 nanoindenter. Successful at measuring adhesion strength between probe-tip and silicon (111).
2. Established that the Hysitron nanoindenter is a quasi-load control device which can only produce sub-nm displacement resolution when probe radius is sufficiently small. Smaller probe radius is necessary to decrease the sudden stiffness change encountered at adhesion zone transition.
3. Bare silicon (111) is an ideal calibration material for sub-10nm measurements. The usual industry calibration standard, quartz, is not repeatable applicable for nanometer-scale displacements found in adhesion studies.

6.2 FUTURE WORK

1. The MEMs-type transducer probe is difficult to clean and limited in available sizes due to expense. The standard transducer probe is simple to clean, can accept custom-tailored probes of various sizes at low expense, but suffers from high surface roughness. The solution is to employ an electrochemical etching process to produce ultra-smooth tungsten tips of custom radii, then use them for nanoindentation testing.
2. Implement nitrogen atmosphere testing of graphene on various substrates.

Appendix

APPENDIX: DMT CONTACT VALIDATION

All reported adhesion results were validated using Hertzian/DMT contact mechanics. The measured force-displacement data for each sample was plotted and then overlaid with a Hertzian fit corresponding to the true modulus of the material. Ideally, this true Hertzian fit will align with the plotted contact data, but generally does not due to cumulative error. A DMT fit is then performed iteratively by varying the material modulus until the curve is aligned with the measured data. The modulus used for the Hertzian and DMT fits can then be compared and the difference is an indicator of experimental error.

Proceeding pages document experimental fit results for quartz, graphite and silicon testing.

Quartz contact data from Hysitron testing using a 50 nm radius probe can be seen in Figure A.1 below. Both the true Hertzian fit and experimental DMT fit agree well, with a difference of 2%. Both curves correspond well to measured force-displacement behavior, this is a low error test.

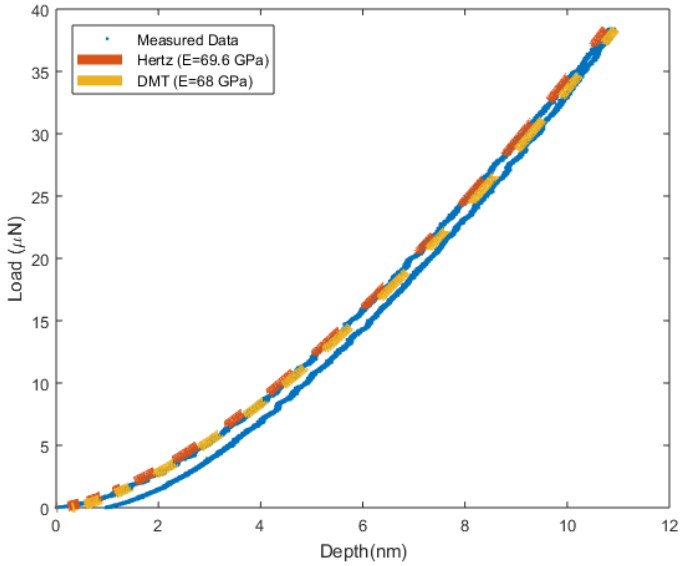

Figure A.1: Hysitron quartz data validation (R=50 nm)

Quartz contact data from UT-Austin testing using a 10 µm radius probe can be seen in Figure A.2 below. Both the true Hertzian fit and experimental DMT fit agree well, with a difference of 1%. Both curves correspond reasonable well to measured force-displacement behavior. There is some departure in the middle of the dataset, but both ends of the curve agree well.

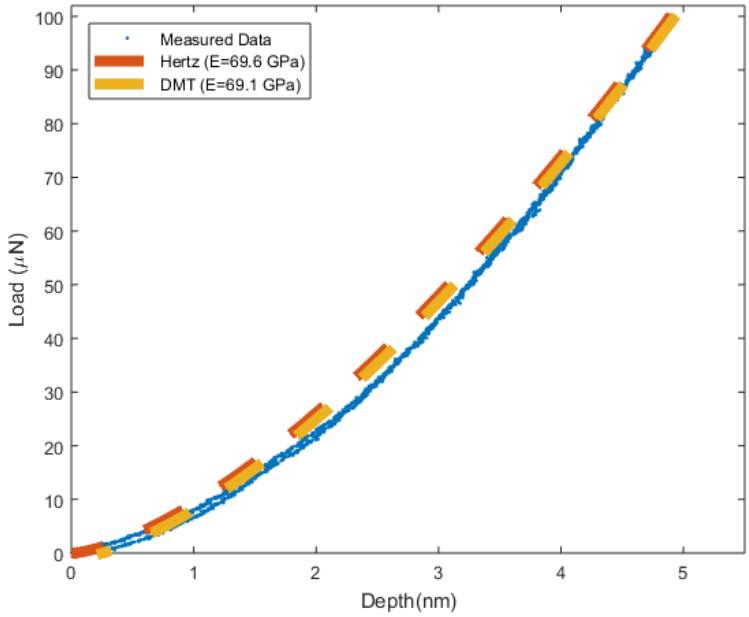

Figure A.2: UT-Austin quartz data validation (R=10 µm)

Graphite contact data from UT-Austin testing using a 10 µm radius probe can be seen in Figure A.3 below. Neither the true Hertzian fit nor experimental DMT correspond well to the measured force displacement data, suggesting that these idealized contact models do not perform well on graphite. Graphite is composed of mono-atomic sheets of carbon atoms and is generally transversely anisotropic. Our suspicion is that carbon sheet sliding, or another atomic scale mechanism could be invalidating the underlying assumptions of the models.

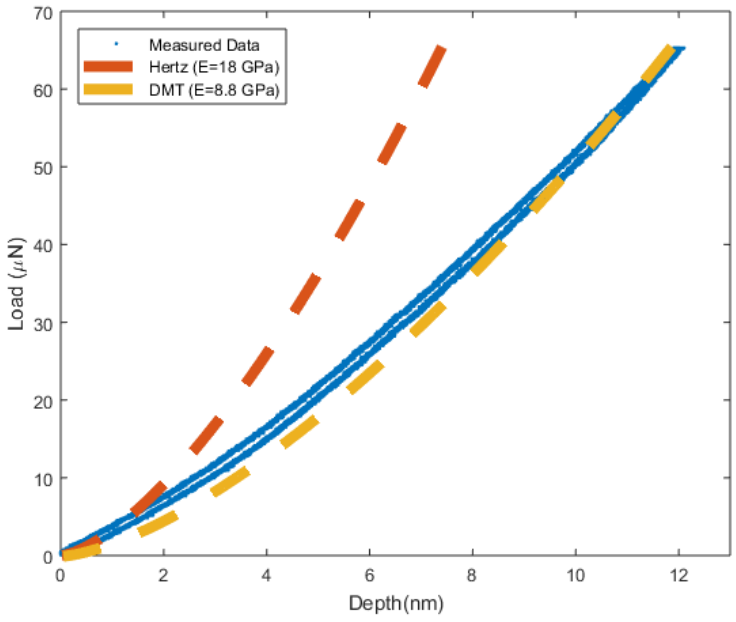

Figure A.3: UT-Austin graphite data validation (R=10 µm)

Silicon contact data from UT-Austin testing using a 10 µm radius probe in ambient environmental conditions can be seen in Figure A.4 below. Neither the true Hertzian fit nor experimental DMT correspond well to majority of measured force displacement data. Changing the environment to nitrogen mix with RH=13% has little to no impact on in-contact data and DMT fit error is very similar. Root cause for deviation from DMT model during contact is unknown, but issue appears consistently on all silicon (111) experiments.

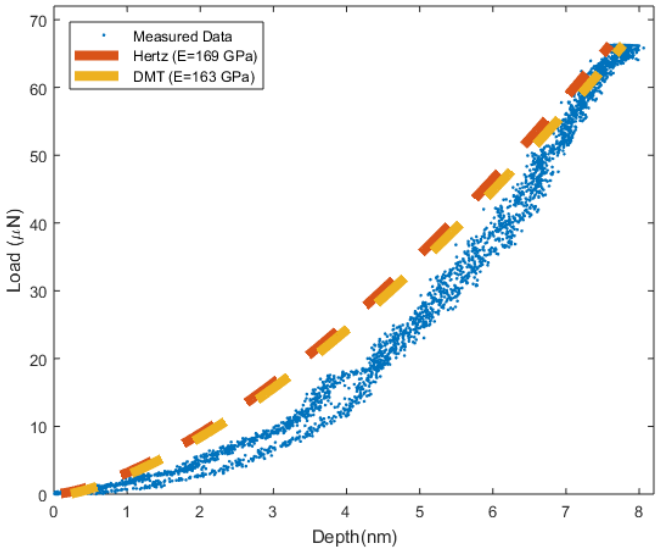

Figure A.4: UT-Austin silicon data validation (R=10 µm)

References

Akiwande, D., Brennan, C.J., Bunch, J.S., Egberts, P., & Felts, J.R. et al., 2017. A review on mechanics and mechanical properties of 2D materials-graphene and beyond. *Extreme Mechanics Letters, 13*, pp. 42-77.

Bae, S., Kim, H., Lee, Y., Xu, X., & Park, J. et al., 2010. Roll-to-roll production of 30-inch graphene films for transparent electrodes. *Nature Nanotechnology, 5*(8), pp.574-578.

Binnig, G., Quate, C.F., Gerber, C., 1986. Atomic force microscope. *Physical Review Letters, 56* (9), pp.930-933

Boddeti, N.G., Koenig, S.P., Long, R., Xiao, J.L., & Bunch, J.S. et al., 2013. Mechanics of adhered pressurized graphene blisters. *Journal of Applied Mechanics, 80*(4), pp.040909.

Bolotin, K., Sikes, K., Jiang, Z., Klima, M., Fudenberg, G., & Hone, J. et al., 2008. Ultrahigh electron mobility in suspended graphene. *Solid State Communications, 146*(9-10), pp.351-355.

Briscoe, W.H., Horn, R.G., 2002. Direct measurement of surface forces due to charging of solids immersed in a nonpolar liquid. *Langmuir, 18*(10), pp.3945-3956.

Brody, T.P., 1984. The thin film transistor – A late blooming flower. *IEEE Transactions on Electron Devices, 31*(11), pp.1614-1628.

Cao, Z., Wang, P., Gao, W., Tao, L., & Suk, J.W. et al., 2014. A blister test for interfacial adhesion of large scale transferred graphene. *Carbon, 69*, pp.147-159.

Cao, Z., Tao, L., Akinwande, D., Huang, R., Liechti, K.M., 2015. Mixed-mode interactions between graphene and substrates by blister tests. *Journal of Applied Mechanics, 82*,pp.0810081-9.

Crabb, R.L., Treble, F.C., 1967. Thin silicon solar cells for large flexible arrays. *Nature, 213*(5082), pp.1223-1224.

Derjaguin, B., Muller, V., & Toporov, Y., 1975. Effect of contact deformations on the adhesion of particles. *Journal of Colloid and Interface Science, 53*(2), pp.314-326.

Field, J.S., Swain, M.V., 1995. Determining the mechanical properties of small volumes of material from submicrometer spherical indentations. *Journal of Materials Research, 10*(1), pp.101-112

Fischer-Cripps, A., 2006. Critical review of analysis and interpretation of nanoindentation test data. *Surface and Coatings Technology, 200*(14-15), pp.4153-4165.

Goertz, M.P., Moore, N.W., 2010. Mechanical of soft interfaces studied with displacement-controlled scanning force microscopy. *Progress in Surface Science, 85*(9-12), pp.347-397.

Grierson, D. S., Flater, E. E., & Carpick, R. W., 2005. Accounting for the JKR–DMT transition in adhesion and friction measurements with atomic force microscopy. *Journal of Adhesion Science and Technology, 19*(3-5), pp.291-311.

Israelachvili, J. (1991). *Intermolecular and Surface Forces* (Second Edition). London: Academic Press.

Israelachvili, J., Min, Y., Akbulut, M., Alig, A., Carver, G., Greene, W., Zeng, H. 2010. Recent advances in the surface forces apparatus (SFA) technique. *Reports on Progress in Physics, 73*(3), pp.036601.

Israelachvili, J., Tabor, D., 1972. The measurement of van der waals dispersion forces in the range 1.5 to 130nm. *Proceedings of the Royal Society of London Series A: Mathematical Physical and Engineering Sciences, 331*(1584), pp.19-38.

Jiang, T., Zhu, Y., 2015. Measuring graphene adhesion using atomic force microscopy with a microsphere tip. *The Royal Society of Chemistry: Nanoscale, 7*(24), pp.10760-10766.

Johnson, K. L. (2004). *Contact mechanics*. Cambridge: Cambridge University Press.

Johnson, K. L., Kendall, K., & Roberts, A. D., 1971. Surface Energy and the Contact of Elastic Solids. *Proceedings of the Royal Society A: Mathematical, Physical and Engineering Sciences, 324*(1558), pp.301-313.

Joyce, S.A., Houston, J.E., 1991. A new force sensor incorporating force-feedback control for interfacial force microscopy. *Review of Scientific Instruments, 62*(3), pp.710-715

Koenig, S.P, Boddeti, N.G., Dunn, M.L., Bunch, J.S., 2011. Ultrastrong adhesion of graphene membranes. *Nature Nanotechnology, 6*(9), pp.543-546.

Lucca, D., Herrmann, K., & Klopfstein, M., 2010. Nanoindentation: Measuring methods and applications. *CIRP Annals - Manufacturing Technology, 59*(2), pp.803-819.

Na, S.R., Suk, J.W., Ruoff, R.S., Huang, R., Liechti, K.M., 2014. Ultra long-range interactions between large area graphene and silicon. *ACS Nano, 8*(11), pp.11234-11242.

Na, S.R., Suk, J.W., Tao, L., Akinwande, D., & Ruoff, R.S. et al, 2015. Selective mechanical transfer of graphene from seed copper foil using rate effects. *ACS Nano, 9*(2), pp.1325-1335.

Nohava, J., Mencik, J., 2012. A contribution to the understanding of low-load spherical indentation – Comparison of tests on polymer and fused silica. *Journal of Materials Research, 27*(1), pp.239-244.

Oliver, W.C., Pharr, G.M., 1992. An improved technique for determining hardness and elastic modulus using load and displacement sensing indentation experiments. *Journal of Materials Research, 7*(6), pp.1564-1583.

Oliver, W.C., Pharr, G.M., 2004. Measurement of hardness and elastic modulus by instrumented indentation: Advances in understanding and refinements to methodology. *Journal of Materials Research, 19*(1), pp.3-20.

Pathak, S., Kalidindi, S., 2015. Spherical nanoindentation stress-strain curves. *Materials Science and Engineering, 91*, pp.1-36.

Restagno, F., Crassous, J., Charlaix, E., Bizonne, C., Monchanin, M., 2002. A new surface forces apparatus for nanorheology. *Review of Scientific Instruments, 73*(6), pp.2292-2297.

Rigby, M**.**, Smith, E.B., Wakeham, W.A., & Maitland, G.C. (1986). *Forces between molecules*. Oxford: Clarendon Press

Suk, J. W., Na, S. R., Stromberg, R. J., Stauffer, D., Lee, J., Ruoff, R. S., & Liechti, K. M., 2016. Probing the adhesion interactions of graphene on silicon oxide by nanoindentation. *Carbon, 103*, pp.63-72.

Tabor, D., Winterton, R. H. S., 1969. The direct measurement of normal and retarded van der Waals forces. P*roceedings of the Royal Society A: Mathematical, Physical and Engineering Sciences, 312*(1511), pp.435-450.

Wang**,** J., Sorescu, D., Seokim, J., Belianinov, A., & Kalinin, S. et al., 2016. Atomic intercalculation to measure adhesion of graphene on graphite. *Nature Communications, 7*(31)

Warren, O.L., Downs, S.A., Wyrobek, T.J., 2004. Challenges and interesting observations associated with feedback-controlled nanoindentation. *International Journal of Materials Research and Advanced Techniques, 95*(5), pp.287-296

Wong, W.S., Salleo, A. (2009). *Flexible Electronics: Materials and Applications*. New York: Springer.

Xin, H. (2013). *Toward Roll-to-roll Transfer of Large Scale Graphene for Flexible Electronics Fabrication* (Master's Thesis). Austin: University of Texas

Yoon, T., Shin, W., Kim, T., Mun, J., & Kim, T. et al., 2012. Direct measurement of adhesion energy of monolayer graphene as-grown on copper and its application to renewable transfer process. *Nano Letters, 12*(3), pp.1448-1452.